Applied Ocean Research 170 (2026) 105060

Contents lists available at ScienceDirect

Applied Ocean Research

journal homepage: www.elsevier.com/locate/apor

Research paper

Bragg scattering of surface gravity waves with periodic porous plates

Huaqing Jin [a,b], Siming Zheng [c], Sichao Qu [a], Xinyi Xie [d], Haicheng Zhang [b,*], Xiaofan Li [a,e,*]

[a] Department of Mechanical Engineering, The University of Hong Kong, 999077, Hong Kong Special Administrative Region of China
[b] College of Mechanical and Vehicle Engineering, Hunan University, Changsha, 410082, China
[c] Ocean College, Zhejiang University, Zhoushan, 316021, China
[d] School of Intelligent Manufacturing Ecosystem, Xi'an Jiaotong-Liverpool University, Taicang, 215412, China
[e] Swire Institute of Marine Science, The University of Hong Kong, Hong Kong Special Administrative Region of China

ARTICLE INFO

Keywords:
Surface gravity wave
Bragg reflection
Thin-walled structure
Porous effect
Wave attenuation

ABSTRACT

In recent years, utilizing periodic structures to control wave propagation has become an active field with broad application prospects. This study presents a novel periodic porous plate structure that integrates the Bragg scattering effect of periodic media with the energy dissipation mechanism of porous materials to attenuate surface gravity waves. A wave-structure interaction model is developed based on linear wave theory and classical porous medium theory, and the associated boundary-value problem is solved using the eigenfunction expansion method. To address the singularity of velocity near the edge of the thin structure, an auxiliary function is introduced to approximate the velocity distribution. The accuracy of the analytical model is verified through convergence analysis, energy conservation validation, and comparisons with existing analytical solutions. Numerical results indicate that the periodic porous plate exhibits Bragg resonance effects, leading to significant wave energy reflection. Furthermore, due to the energy dissipation induced by the porosity, the porous plate model presents superior wave attenuation performance than the solid plate model, particularly in non-Bragg resonance regions where the enhancement is more pronounced. Multi-parameter analysis shows that the model can achieve nearly complete wave energy dissipation under specific conditions and reveals that the peak reflection of Bragg resonance is affected by wave conditions but remains independent of the lattice constant. Additionally, the presence of porosity effectively reduces the hydrodynamic load on the plate. These findings may offer valuable technological insights for water wave energy utilization and coastal protection.

1. Introduction

In 1913, while studying the diffraction of X-rays in crystals, Bragg observed that when the distance between the crystals was exactly an integer multiple of the half-wavelength of X-rays, extremely strong resonant reflection occurred, and the X-rays could not pass through the crystals. This phenomenon is also known as 'Bragg reflection' (Bragg and Bragg, 1913). Later, researchers applied the principle of Bragg reflection to design structures with photonic bandgaps (Yablonovitch and Gmitter, 1989). By arranging materials with different refractive indices in a periodic pattern, and when the spatial period matches the wavelength of light, Bragg scattering induced by the periodicity generates photonic band gaps within a certain frequency range. If the energy level of photons falls within the frequency range of this bandgap, they cannot propagate through the medium. Further research has shown that structures with phononic bandgaps can be fabricated using composite materials with periodically repeating elastic moduli (Kushwaha et al., 1993). Bragg resonance effects occur in periodic structures, allowing for the creation of bandgap in the acoustic wave frequency range. The use of periodic structures to control the propagation of electromagnetic waves or elastic waves has become an active field in contemporary scientific research, with vast potential for applications (Ma and Sheng, 2016; B. Wu et al., 2024).

Water waves, as surface waves with both transverse and longitudinal wave characteristics, share similar propagation properties with traditional mechanical waves. In 1982, Davies (1982) theoretically calculated the interaction between water waves and sinusoidal seabed topography, and found strong reflection occurs when the wavenumber of the seabed undulation is twice of that the surface water waves. Heathershaw (1982) conducted physical experiments on the interaction between surface gravity waves and undulating seabed topography, and the experiments revealed that when the wavelength of the periodic topography is half of the surface wave's wavelength, a significant amount of wave energy is reflected back, confirming the existence of Bragg resonance effects in water wave periodic structures. Torres

* Corresponding authors.
E-mail addresses: zhanghc@hnu.edu.cn (H. Zhang), lixf@hku.hk (X. Li).

https://doi.org/10.1016/j.apor.2026.105060
Received 20 November 2025; Received in revised form 7 March 2026; Accepted 7 April 2026
Available online 8 April 2026

et al. (1999) were the first to visually demonstrate Bloch water waves, proving that water waves exhibit band structures similar to those of electromagnetic and acoustic waves. Bandgaps may exist between the passbands, within which wave propagation is forbidden. The forbidden band effect caused by Bragg resonance offers a powerful solution for wave attenuation in the field of ocean engineering (Zhu et al., 2024; Jin et al., 2024a).

Over the past few decades, numerous theoretical and experimental studies have been conducted on the interaction between water waves and periodic structures. In terms of theoretical research, Mei (1985) used the method of multiple-scale perturbation to study the Bragg scattering of shallow water waves and sandbar topography, explaining the formation of nearshore sandbars parallel to the coast and their association with Bragg resonance reflection. Porter and Porter (2003) investigated Bragg scattering of water waves on finite periodic topographies and Bloch wave problems on infinite periodic topographies, deriving the exact solution for periodic topography scattering based on full linear theory and Galerkin approximation. Based on shallow water wave theory, Chang and Liou (2007) studied the interaction between long water waves and trapezoidal bars. They derived a shape transfer function to determine the wave reflection and transmission, discovering phase shifts in Bragg resonance induced by the geometry of the bar. Ning et al. (2022) studied nonlinear Bragg reflection on periodic topographies, and for the first time confirmed the existence of fourth-order subharmonic Bragg resonance and first-order Bragg resonance induced by second-order transmitted waves. They revealed the impact of primary structural parameters and nonlinearity of free surface waves on the characteristics of third-order Bragg resonance. Cui et al. (2023) developed a numerical method based on the Rankine source integral equation to solve the eigenvalue problem for infinite periodic scatterers, and investigated the effect of convex parabolic, concave parabolic, sine, and cylindrical scatterer structures on Bragg resonance bandgap. Q. Wu et al. (2024) studied the Bragg resonance effect of nonlinear focusing wave groups by periodic seabed topography, developing an efficient fully nonlinear numerical model using conformal mapping to simulate the interaction between waves and topography. The analysis found that, due to nonlinear effects at the free surface, the amplitude increase of the wave group slightly weakens the Bragg reflection and causes resonance shift phenomena. Liu et al. (2025) studied the zero-reflection phenomenon in Bragg resonance, analyzing the zero reflection characteristics of surface gravity waves propagating through finite periodic arrays of parabolic, modified cosine, semicircular, and trapezoidal embankments, revealing the total number of zero reflections between any two adjacent Bragg resonance peaks and their distribution patterns. In terms of experimental studies, Hsu et al. (2001) conducted a series of experiments on periodic sandbars placed on the seabed, investigating the propagation changes of water waves through rectangular, triangular, and sinusoidal sandbars, and testing the effects of sandbar number, spacing, width, height, and wave conditions on the Bragg reflection. Cho et al. (2004) carried out a study on the reflection of regular water waves by periodic rectangular and trapezoidal bars, recommending the trapezoidal shape for practical application. Liu et al. (2016) investigated the Bragg reflection of water waves by multiple submerged semicircular breakwaters, using multipole expansion combined with polar coordinate transformations to develop a fully linear potential flow solution. They experimentally measured the reflection and transmission coefficients of breakwaters at different wave periods and structural spacings, verifying the theoretical analysis results. Xu et al. (2025) proposed an optimized layout of oyster reefs based on Bragg resonance to promote optimal oyster growth and enhance wave attenuation capabilities, demonstrating through experiments that compared to adjacent layouts, the optimized layout based on Bragg resonance improves wave attenuation performance by 27%.

In the field ocean engineering, there has been an increasing amount of research on porous breakwaters and perforated breakwaters for water wave attenuation. These structures are made of porous materials or incorporate artificial perforations, allowing water to pass through their hulls and thereby dissipating wave energy. For example, Ji et al. (2016) developed a new type of breakwater by installing net cages on the top of the rectangular breakwater, where the porous net can serve as auxiliary structures to further interfere with the incident waves. Neelamani et al. (2017) proposed a double-layered slotted wall breakwater by introducing holes in the side walls of the traditional box-type breakwater, achieving better wave attenuation performance than the box-type breakwater. Qiao et al. (2018) studied the scattering of water waves by a floating body with two vertical attached porous walls and found the transmission coefficient was significantly influenced by the porous properties of the attached vertical walls. Overall, these studies have shown that porous structures can provide enhanced wave attenuation due to their energy dissipation capability (Han and Wang, 2022). Additionally, the porous structure has other advantages, such as allowing water circulation, which is beneficial to the marine ecological environment (Halvorson and Huang, 2024; Reyes et al., 2024). Recent research has further expanded this field to include more complex configurations, such as Bragg scattering by submerged breakwater arrays (Vijay et al., 2021), the hydrodynamic performance of vertical wall-type structures with slotted barriers (Kumaran et al., 2025), and the hydroelastic interaction between floating elastic plates and porous barriers (Praveen et al., 2022; Sahoo et al., 2025).

However, the combination of the Bragg scattering effect of periodic media with the energy dissipation mechanism of porous materials has received limited attention in the field of fluid dynamics. Moreover, most existing theoretical and experimental research has primarily focused on larger-scale structures, with little attention given to thin-walled structures. From a cost perspective, thin-walled structures are advantageous due to their small scale (with thickness approaching zero), resulting in lower material costs. Furthermore, in terms of construction difficulty, thin-walled structures are lightweight and easier to install (Zheng et al., 2022). Therefore, based on the periodic effect and the dissipation mechanism, this study proposes a novel Bragg scattering structure composed of periodically arranged porous thin plates for ocean wave attenuation. Undoubtedly, the design of porous structures leads to more complex fluid–structure interactions, making the problem-solving process more challenging (Chanda and Pramanik, 2023; Qiao et al., 2020). Furthermore, the thin-walled nature of the structure introduces new challenges in solving this interaction: singularities may occur in fluid velocity at the edges of the thin structures. These singularities complicate the process of obtaining exact analytical solutions to related hydrodynamic problems (Liang et al., 2023).

The primary objectives of this study are: (i) to develop a rigorous analytical model for the interaction between surface gravity waves and an array of periodic porous thin plates; (ii) to investigate the modification of Bragg resonance by the introduction of energy dissipation; and (iii) to evaluate the performance of these structures as a sustainable coastal protection measure. By separating the underlying physics from the practical application, the scope of this work is to understand the fundamental wave–structure interaction within a periodic porous system and to design a lightweight, cost-effective waveguide capable of reducing wave transmission and hydrodynamic loads. It should be noted that the present analytical model assumes all porous plates to be strictly rigid and stationary, thereby excluding any structural motion. In practical scenarios, the dynamic responses or flexibility of the structures could introduce additional fluid–structure interactions, which may further influence the Bragg resonance characteristics and the resulting hydrodynamic loads.

The remainder of this paper is organized as follows. In Section 2, the boundary conditions for wave propagation in this system are first described, with the porous medium modeled using linear pressure loss boundary conditions (Yu and Chwang, 1994). The general solution for the wave velocity potential is then obtained using the method of separation of variables. To address the velocity singularity at the edge of the plate, an auxiliary function is introduced to approximate the local

Table 1
Nomenclature.

Symbol	Description	Symbol	Description
Roman symbols		P_{diss}	Total dissipation power
A	Wave amplitude	P_{inc}	Power of the incident wave
b_n	Physical thickness of the nth plate	R	Reflection coefficient
c_g	Group velocity	s_n	Inertia coefficient
C_n^M	Added mass coefficient	$S_i(f)$	Incident wave spectrum
d_n	Submergence depth of the nth plate	$S_r(f), S_t(f)$	Reflected and transmitted wave spectra
D	Dissipation coefficient	t	Time
$E_{n,q,j}$	Integral identity coefficient	T	Transmission coefficient
r_n	Linearized resistance coefficient	T_{2q}	Chebyshev polynomial of the first kind
f	Wave frequency	Z_j	Vertical eigenfunction
f_p	Peak wave frequency	$\overline{C}_r$	Mean reflection coefficient
$F_{e,n}$	Horizontal wave force	$\overline{C}_t$	Mean transmission coefficient
g	Gravitational acceleration	$\overline{C}_d$	Mean dissipation coefficient
G_n	Complex porosity parameter		
h	Constant water depth	**Greek symbols**	
H_s	Significant wave height	ϵ_n	Porosity of the nth plate
i	Imaginary unit	η^I	Incident wave surface elevation
J_{2q}	Bessel function of order $2q$	λ_j	Roots of the dispersion relation
k	Wavenumber	ρ	Water density
L	Lattice constant	ϕ, Φ	Velocity potential
l_n	Length of the nth plate	ω	Angular frequency
N	Total number of plates	γ	Peak enhancement factor
Other symbols			
Γ_n^P	Domain of the nth porous plate	∇	Gradient operator
Γ_n^G	Domain of the gap above the nth plate	Ω_n	nth fluid subregion

velocity distribution. The unknown coefficients in the velocity potential and auxiliary function are determined through continuity conditions. Section 3 presents numerical examples to illustrate the characteristics of the proposed model. First, the validity of the analytical solution is verified from several aspects. Then, the propagation characteristics of regular water waves through periodically arranged solid and porous plates are compared and analyzed. The influence of key parameters, including porosity, plate length, and lattice parameters, is also studied. Finally, Section 4 summarizes the main findings of this research and outlines potential directions for future studies.

2. Mathematical model

This section establishes the mathematical model for the interaction between water waves and a periodic array of porous thin plates. Linear wave theory is employed to describe the fluid flow and the associated wave motion, with the assumption that the submerged porous plates remain stationary under the action of the water waves. The symbols used in the mathematical model and their corresponding definitions are provided in Table 1.

2.1. Boundary-value problem

This study focuses on a periodic array of thin porous plates subjected to regular incident waves with small wave steepness. The plates are submerged in the fluid domain Ω with a constant depth h and infinite horizontal extent, as shown in Fig. 1. A two-dimensional Cartesian coordinate system Oxz is established to mathematically characterize the problem, with the x-coordinate aligned with the still water surface and the z-coordinate pointing vertically upwards. Each plate has a length l_n and negligible thickness, and is vertically mounted on the seabed at the location $x = x_n$, where $n \in \{1, 2, \ldots, N\}$. The area occupied by each plate is defined by the set of points $\Gamma_n^P = \{(x_n, z) \mid -h < z < -d_n\}$, where $d_n = h - l_n$ is the submergence depth of the nth plate. To facilitate subsequent analysis, the gap above the nth plate is also defined as $\Gamma_n^G = \{(x_n, z) \mid -d_n < z < 0\}$.

Assuming the fluid is inviscid, incompressible, and undergoes irrotational motion, the fluid flow within the water domain can be described by the velocity potential as

$$\Phi(x, z, t) = \mathrm{Re}\left[\phi(x, z)\mathrm{e}^{-\mathrm{i}\omega t}\right] \tag{1}$$

where i represents the imaginary unit, ω denotes the angular frequency, t is time, and ϕ is the spatial complex velocity potential, which is independent of time.

The spatial function ϕ must satisfy the Laplace equation

$$\frac{\partial^2\phi(x, z)}{\partial x^2} + \frac{\partial^2\phi(x, z)}{\partial z^2} = 0 \tag{2}$$

within the fluid domain Ω, and must satisfy the impermeable condition at the seabed:

$$\frac{\partial\phi(x, z)}{\partial z} = 0, \quad z = -h. \tag{3}$$

At the free surface, the potential is related to the surface elevation through dynamic and kinematic conditions. These can be combined into a single boundary condition as

$$\frac{\partial\phi(x, z)}{\partial z} = \frac{\omega^2}{g}\phi, \quad z = 0, \tag{4}$$

where $g \approx 9.81\ \mathrm{m/s^2}$ is the gravitational acceleration.

Assuming that the normal velocity of the water particle at the surface of the porous plates is proportional to the pressure difference between the two sides of the plate (i.e., Darcy's law) (Yu and Chwang, 1994), the boundary condition on the plate is given by

$$\left.\frac{\partial\phi(x, z)}{\partial x}\right|_{x=x_n^-} = \left.\frac{\partial\phi(x, z)}{\partial x}\right|_{x=x_n^+} = \mathrm{i}kG_n\left[\phi\left(x_n^-, z\right) - \phi\left(x_n^+, z\right)\right], \quad (x, z) \in \Gamma_n^P \tag{5}$$

for all $n = 1, 2, \ldots, N$, where x_n^- and x_n^+ represent the left and right sides of plate n, respectively. k is the wavenumber of the propagating wave, which satisfies the dispersion relation $\omega^2 = gk\tanh(kh)$. G_n denotes the complex porosity parameter of the plate n, defined as

$$G_n = \frac{\epsilon_n}{kb_n(r_n - \mathrm{i}s_n)}, \tag{6}$$

where b_n is the physical thickness of the plate n, r_n is the linearized resistance coefficient, s_n represents the coefficient of the inertial force coefficient acting on the porous plate and ϵ_n denotes the porosity (Yu, 1995).

Regarding the linearized resistance coefficient r_n for vertical porous plate, Li et al. (2006) derived an empirical formula by analyzing the

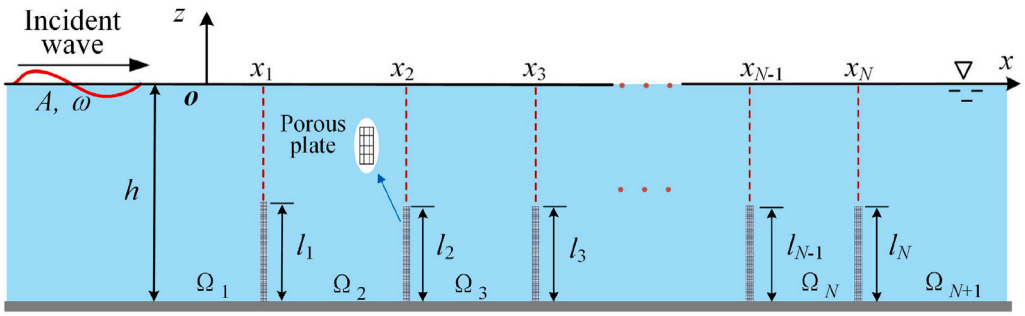

Fig. 1. Sketch of water waves interacting with periodic porous plates.

experimental data,

$$r_n = -3338.7(\frac{b_n}{h})^2 + 82.67\frac{b_n}{h} + 8.7111, \quad 0.0097 \le \frac{b_n}{h} \le 0.05\,. \tag{7}$$

The inertia coefficient s_n is given by

$$s_n = 1 - \frac{1-\epsilon_n}{\epsilon_n} C_n^M\,, \tag{8}$$

where C_n^M is the added mass coefficient of the porous medium. In many studies, $C_n^M = 0$, (or $s_n = 1$) is frequently adopted through comparisons between numerical predictions and experimental results (Zhu and Chwang, 2001; Molin, 2011; Suh et al., 2011).

For simplicity, let $G_n = \Re(G_n) + \mathrm{i}\Im(G_n)$, the real part of G_n corresponds to the resistance effect of the porous material, while the imaginary part represents the inertial effect of the fluid within the porous medium.

The Sommerfeld radiation condition must also be satisfied to ensure that the scattered waves can propagate away from the array:

$$\lim_{x\to\pm\infty}\left(\frac{\partial}{\partial x} \mp \mathrm{i}k\right)\left(\phi - \phi^I\right) = 0\,, \tag{9}$$

where ϕ^I is the velocity potential associated with the incident wave.

Additionally, the submerged edges of the plates, located at $(x_n, -d_n)$, introduce singularities of order $-1/2$ in the fluid velocity, requiring that

$$\left((x-x_n)^2 + (z+d_n)^2\right)^{1/2} \nabla\phi \to 0 \quad \text{as} \quad \left((x-x_n)^2 + (z+d_n)^2\right)^{1/2} \to 0\,. \tag{10}$$

2.2. General expressions of velocity potentials

Considering a regular incident wave propagating to the right with small amplitude A and wavenumber k, the time-independent wave surface is given by

$$\eta^I(x) = Ae^{\mathrm{i}kx}\,. \tag{11}$$

The incident wave satisfies the Laplace equation in Eq. (2), the free-surface boundary condition in Eq. (4), and the seabed boundary condition in Eq. (3), which leads to the incident potential

$$\phi^I = -\frac{\mathrm{i}gA}{\omega\cosh(kh)} e^{\mathrm{i}kx}\cosh(k(z+h))\,. \tag{12}$$

When the incident waves pass over the arrayed structures, diffracted waves are generated, and the total wave velocity potential is the sum of the incident potential ϕ^I and the diffraction potential ϕ^D,

$$\phi = \phi^I + \phi^D\,. \tag{13}$$

The eigenfunction expansion method is used to find the solution for the diffracted potentials. First, the entire fluid domain Ω can be divided into $N+1$ subregions by N plates, as shown in Fig. 1. These subregions can be described as

$$\begin{cases} \Omega_1 = \{(x,z) \mid x < x_1,\ z \in (-h,0)\}, \\ \Omega_n = \{(x,z) \mid x \in (x_{n-1}, x_n),\ z \in (-h,0)\}, \quad n = 2,\dots,N, \\ \Omega_{N+1} = \{(x,z) \mid x > x_N,\ z \in (-h,0)\}. \end{cases} \tag{14}$$

Then, according to the upper and lower boundary conditions of each subdomain, as well as the Sommerfeld radiation condition at the far-field subdomains, the general solutions for ϕ^D in the three types of subdomains are deduced as

$$\begin{cases} \phi_1^D = \sum_{j=0}^{\infty} A_{1,j} e^{\lambda_j(x-x_1)} Z_j(z), \quad (x,z) \in \Omega_1, \\ \phi_n^D = \sum_{j=0}^{\infty} \left(A_{n,j} e^{\lambda_j(x-x_n)} + B_{n,j} e^{-\lambda_j(x-x_n)}\right) Z_j(z), \\ \quad (x,z) \in \Omega_n,\ n = 2,3,\dots,N, \\ \phi_{N+1}^D = \sum_{j=0}^{\infty} B_{N+1,j} e^{-\lambda_j(x-x_{N+1})} Z_j(z), \quad (x,z) \in \Omega_{N+1}. \end{cases} \tag{15}$$

where $A_{1,j}, A_{n,j}, B_{n,j}, B_{N+1,j}, (j = 0,1,2,\dots)$ are the unknown coefficients to be determined, and x_{N+1} is the envisioned location, set as $x_{N+1} = x_N$.

The depth-dependent function (eigenfunction) $Z_j(z)$ in Eq. (15) is defined as follows:

$$Z_j(z) = N_j^{-1/2}\cos\left(\lambda_j(h+z)\right), \quad N_j = \frac{2\lambda_j h + \sin\left(2\lambda_j h\right)}{4\lambda_j h}, \quad j \in \mathbb{N}^+ \cup \{0\}\,, \tag{16}$$

where λ_j is the positive real root of the following dispersion relation:

$$\omega^2/g + \lambda_j \tan\left(\lambda_j h\right) = 0, \quad j \in \mathbb{N}^+ \cup \{0\}\,, \tag{17}$$

with $\lambda_0 = -\mathrm{i}k$ corresponding to the progressive wave mode, and $\lambda_j \in \mathbb{R}^+$ for $j > 0$, which is related to the evanescent wave mode. The eigenfunction $Z_j(z)$ satisfies the orthogonality relation:

$$\int_{-h}^{0} Z_j(z) Z_\zeta(z)\,\mathrm{d}z = h\delta_{j,\zeta}, \tag{18}$$

where $\delta_{j,\zeta}$ is the Kronecker delta function, defined as

$$\delta_{j,\zeta} = \begin{cases} 1, & j = \zeta \\ 0, & j \ne \zeta \end{cases}\,. \tag{19}$$

2.3. Method of computation for unknown coefficients

2.3.1. Auxiliary velocity distribution functions

The unknown coefficients in Eq. (15) can be determined using the standard eigenfunction expansion method at the interfaces between adjacent subregions. However, the sharp edges of the thin plates introduce velocity singularities, resulting in an ill-conditioned matrix that hampers convergence. To address this issue, the Galerkin approximation method developed by Porter and Evans (1995) is employed. The following auxiliary functions are constructed to represent the horizontal velocity in the gap above the nth plate:

$$U_n(z) = \sum_{q=0}^{\infty} U_{n,q} u_{n,q}(z), \quad -d_n \le z \le 0\,. \tag{20}$$

where $U_{n,q}$ is the unknown coefficient to be determined. The horizontal velocity component $U_n(z)$ should satisfy the free-surface condition of

Eq. (4) and the convergence condition of Eq. (10). Thus, the auxiliary function is given by

$$\tilde{u}_{n,q}(z) = u_{n,q}(z) - \frac{\omega^2}{g}\int_{-d_n}^{z} u_{n,q}(\tau)\,\mathrm{d}\tau, \tag{21}$$

in which

$$\tilde{u}_{n,q}(z) = \frac{2(-1)^q}{\pi\sqrt{d_n^2 - z^2}} T_{2q}\left(-\frac{z}{d_n}\right), \tag{22}$$

where $T_{2q}(z/d_n)$ represents the Chebyshev polynomial of the first kind of order $2q$.

The auxiliary function satisfies the following integral identity:

$$E_{n,q,j} = \int_{-d_n}^{0} u_{n,q}(z) Z_j(z)\,\mathrm{d}z = N_j^{-1/2}\cos\left(\lambda_j h\right) J_{2q}\left(\lambda_j d_n\right). \tag{23}$$

in which $J_{2q}(\lambda_j d_n)$ is the Bessel function of order $2q$.

2.3.2. Continuity conditions

After introducing the auxiliary velocity functions, the unknown coefficients can be solved using the eigenfunction expansion method. The continuity conditions at the common interface $x = x_n$ between adjacent subdomains are given as

$$\left.\frac{\partial\phi_n^D}{\partial x}\right|_{x=x_n^-} = \begin{cases} U_n(z), & (x,z)\in\Gamma_n^G \\ -\left.\frac{\partial\phi^I}{\partial x}\right|_{x=x_n} + \mathrm{i}kG_n\left(\left.\phi_n^D\right|_{x=x_n^-} - \left.\phi_{n+1}^D\right|_{x=x_n^+}\right), & (x,z)\in\Gamma_n^P, \end{cases} \tag{24}$$

$$\left.\frac{\partial\phi_{n+1}^D}{\partial x}\right|_{x=x_n^+} = \begin{cases} U_n(z), & (x,z)\in\Gamma_n^G \\ -\left.\frac{\partial\phi^I}{\partial x}\right|_{x=x_n} + \mathrm{i}kG_n\left(\left.\phi_n^D\right|_{x=x_n^-} - \left.\phi_{n+1}^D\right|_{x=x_n^+}\right), & (x,z)\in\Gamma_n^P, \end{cases} \tag{25}$$

$$\left.\phi_n^D\right|_{x=x_n^-} = \left.\phi_{n+1}^D\right|_{x=x_n^+}, \quad (x,z)\in\Gamma_n^G. \tag{26}$$

Eqs. (24) and (25) are the continuity conditions for velocity, and Eq. (26) is the continuity condition for pressure.

2.3.3. Solution of unknown coefficients

After inserting the expression of ϕ^D in each subdomain as given in Eq. (15) into Eqs. (24) and (25), multiplying by $Z_\zeta(z)$ and integrating the resulting equations over $[-h, 0]$, we obtain

$$\begin{aligned} &\left(A_{n,\zeta} - \bar{\delta}_{n,1}B_{n,\zeta}\right)\lambda_\zeta h - \sum_{q=0}^{\infty} U_{n,q}E_{n,q,\zeta} \\ &- \mathrm{i}kG_n\sum_{j=0}^{\infty}\left(A_{n,j} + \bar{\delta}_{n,1}B_{n,j}\right)Q_{n,j,\zeta} \\ &+ \mathrm{i}kG_n\sum_{j=0}^{\infty}\left(\bar{\delta}_{n,N+1}A_{n+1,j}e^{\lambda_j D_n} + B_{n+1,j}e^{-\lambda_j D_n}\right)Q_{n,j,\zeta} \\ &= -\frac{gAke^{\mathrm{i}kx_n}P_{n,0,\zeta}}{\omega\cosh(kh)\sqrt{N_\zeta}} \end{aligned} \tag{27}$$

and

$$\begin{aligned} &-\sum_{q=0}^{\infty} U_{n,q}E_{n,q,\zeta} + \left(\bar{\delta}_{n,N+1}A_{n+1,\zeta}e^{\lambda_\zeta D_n} - B_{n+1,\zeta}e^{-\lambda_\zeta D_n}\right)\lambda_\zeta h \\ &- \mathrm{i}kG_n\sum_{j=0}^{\infty}\left(A_{n,j} + \bar{\delta}_{n,1}B_{n,j}\right)Q_{n,j,\zeta} \\ &+ \mathrm{i}kG_n\sum_{j=0}^{\infty}\left(\bar{\delta}_{n,N+1}A_{n+1,j}e^{\lambda_j D_n} + B_{n+1,j}e^{-\lambda_j D_n}\right)Q_{n,j,\zeta} \\ &= -\frac{gAke^{\mathrm{i}kx_n}P_{n,0,\zeta}}{\omega\cosh(kh)\sqrt{N_\zeta}} \end{aligned} \tag{28}$$

After inserting the expression of ϕ^D in each subdomain as given in Eq. (15) into Eq. (26), multiplying by $U_\zeta(z)$ and integrating the resulting equations over $[-d_n, 0]$, we obtain

$$\sum_{j=0}^{\infty}\left(A_{n,j} + \bar{\delta}_{n,1}B_{n,j}\right)E_{n,\zeta,j} = \sum_{j=0}^{\infty}\left(\bar{\delta}_{n,N}A_{n+1,j}e^{\lambda_j D_n} + B_{n+1,j}e^{-\lambda_j D_n}\right)E_{n,\zeta,j} \tag{29}$$

In Eqs. (27), (28), and (29), the function $\bar{\delta}_{n,j} = 1 - \delta_{n,j}$, the quantity $D_n = x_n - x_{n+1}$, and $P_{n,j,\zeta}$ equals

$$P_{n,j,\zeta} = \begin{cases} \frac{2\lambda_\zeta l_n + \sin(2\lambda_\zeta l_n)}{4\lambda_\zeta}, & \zeta = j \\ \frac{1}{2}\left(\frac{\sin[(\lambda_j+\lambda_\zeta)l_n]}{\lambda_j+\lambda_\zeta} + \frac{\sin[(\lambda_j-\lambda_\zeta)l_n]}{\lambda_j-\lambda_\zeta}\right), & \zeta \neq j \end{cases}, \tag{30}$$

and $Q_{n,j,\zeta} = P_{n,j,\zeta}/\sqrt{N_j N_\zeta}$.

A linear algebraic system can be formed from Eqs. (27), (28), and (29), which can be used to solve the unknown coefficients $A_{1,j}$, $A_{n,j}$, $B_{n,j}$, $B_{N+1,j}$, and $U_{n,j}$ numerically, after truncating the infinite terms of $Z_j(z)$ and $u_{n,q}(z)$. Specifically, $Z_j(z)$ and $u_{n,q}(z)$ can be truncated at the orders $j = J$ and $q = Q$, respectively. A set of linear equations of dimension $(2J + Q + 3)N$ will be generated, and the same number of unknowns can be solved.

2.4. Hydrodynamic quantities

2.4.1. Wave force acting on the plate

The excitation force exerted by waves on the plate can be obtained by integrating the pressure over its surface area. Based on Bernoulli's law, the horizontal wave force acting on plate n is expressed as

$$\begin{aligned} F_{e,n} &= \mathrm{i}\omega\rho\int_{-h}^{-d_n}\left[\phi|_{x=x_n^-} - \phi|_{x=x_n^+}\right]\mathrm{d}z \\ &= \mathrm{i}\omega\rho\left[\sum_{j=0}^{\infty}\left[\left(A_{n,j} + \bar{\delta}_{n,1}B_{n,j}\right) - \left(\bar{\delta}_{n,N}A_{n+1,j}e^{\lambda_j D_n} + B_{n+1,j}e^{-\lambda_j D_n}\right)\right]G_{n,\zeta}\right], \end{aligned} \tag{31}$$

in which

$$G_{n,\zeta} = \frac{\sin\left[\lambda_\zeta\left(h - d_n\right)\right]}{\sqrt{N_\zeta}\lambda_\zeta}. \tag{32}$$

2.4.2. Wave reflection and transmission coefficients

The reflection coefficient R is the ratio of the amplitude of the diffracted wave η^D to the amplitude of the incident wave η^I, and it can be obtained by computing the wave amplitudes at the radiation boundary $x = -\infty$:

$$R = \left|\frac{\eta^D}{\eta^I}\right|_{z=0,x=-\infty} = \left|\frac{\mathrm{i}\omega Z_0(0)A_{1,0}e^{\mathrm{i}kx_1}}{gA}\right|. \tag{33}$$

The transmission coefficient T is the ratio of the amplitude of the transmitted wave to the amplitude of the incident wave, and it can be evaluated by calculating the wave amplitudes at the radiation boundary $x = +\infty$:

$$T = \left|\frac{\eta^D + \eta^I}{\eta^I}\right|_{z=0,x=\infty} = \left|1 + \frac{\mathrm{i}\omega Z_0(0)B_{N+1,0}e^{-\mathrm{i}kx_{N+1}}}{gA}\right|. \tag{34}$$

2.4.3. Wave power dissipation

Direct method. Due to the resistance effect of the porosity, wave energy is dissipated by the porous plates as the waves pass through them. The time-averaged energy dissipated by the plate can be straightforwardly calculated by integrating the power dissipated per unit area over the plate. The energy dissipation caused by plate i is given by

$$P_i = \frac{\rho\omega k}{2}\mathrm{Re}(G_i)\int_{-h}^{d_i}\left|\phi_{x=x_i^+} - \phi_{x=x_i^-}\right|^2\mathrm{d}z = \frac{\rho\omega k}{2}\mathrm{Re}(G_i)S_i, \tag{35}$$

where

$$S_i = \left[\sum_{m=0}^{\infty} \sum_{n=0}^{\infty} b_m^i b_n^{i^*} Q_{i,m,n} + \sum_{m=0}^{\infty} \sum_{n=0}^{\infty} c_m^i c_n^{i^*} Q_{i,m,n} - \sum_{m=0}^{\infty} \sum_{n=0}^{\infty} \left(c_m^i b_n^{i^*} + b_m^i c_n^{i^*} \right) Q_{i,m,n} \right], \tag{36}$$

where the superscript $(*)$ denotes complex conjugation, and

$$c_m^i = A_{i,m} + \bar{\delta}_{i,1} B_{i,m}, \quad b_m^i = \bar{\delta}_{i,N} A_{i+1,m} e^{\lambda_j D_i} + B_{i+1,m} e^{-\lambda_j D_i}. \tag{37}$$

The total dissipation power of the N plates is

$$P_{\text{diss}} = \sum_{i=1}^{N} P_i. \tag{38}$$

The power produced by the incident wave is

$$P_{\text{inc}} = \frac{1}{2} \rho g A^2 c_g, \tag{39}$$

where $c_g = \mathrm{d}\omega/\mathrm{d}k$ is the group velocity of the wave, and

$$c_g = \frac{\omega}{2k} \left[1 + \frac{2kh}{\sinh(2kh)} \right]. \tag{40}$$

Thus, the dissipation efficiency of the porous plate array can be computed as

$$D = \frac{P_{\text{diss}}}{P_{\text{inc}}} = \frac{2k^2 \sinh(2kh)}{gA^2 \left[\sinh(2kh) + 2kh \right]} \sum_{i=1}^{N} \mathrm{Re}(G_i) S_i. \tag{41}$$

Indirect method. Apart from the direct method, the energy dissipation can be derived based on Green's theorem (Falnes and Kurniawan, 2020):

$$P_{\text{diss}} = \frac{\rho\omega}{4\mathrm{i}} \int_{-h}^{0} \left[\left(\phi \frac{\partial \phi^*}{\partial x} - \phi^* \frac{\partial \phi}{\partial x} \right) \Big|_{x=\infty} - \left(\phi \frac{\partial \phi^*}{\partial x} - \phi^* \frac{\partial \phi}{\partial x} \right) \Big|_{x=-\infty} \right] \mathrm{d}z. \tag{42}$$

After further derivation, Eq. (42) can be rewritten as

$$P_{\text{diss}} = -\frac{\rho\omega(\sinh kh \cosh kh + kh)}{4 \cosh^2 kh} \times \left(\left| B_{N+1,0} e^{-\mathrm{i}kx_{N+1}} Z_0(0) - \frac{\mathrm{i}gA}{\omega} \right|^2 - \left| \frac{\mathrm{i}gA}{\omega} \right|^2 + \left| A_{1,0} e^{\mathrm{i}kx_1} Z_0(0) \right|^2 \right). \tag{43}$$

Using the definition of the dissipation coefficient from Eq. (41), we obtain

$$D = \frac{P_{\text{diss}}}{P_{\text{inc}}} = 1 - \left(R^2 + T^2 \right), \tag{44}$$

which is in accordance with the principle of energy conservation, indicating that the energy of the incident wave is reflected, transmitted, and dissipated by the porous plates.

3. Results and discussion

In the following section, we focus on the scattering characteristics of periodic porous plates for regular water waves. The validity of the analytical model was first verified. Then, the performance differences between solid and porous plates were compared. Subsequently, studies of the influence of various parameters were conducted. In the analysis that followed, the spacing between adjacent plates (lattice constant) was denoted by L. The subscript n in l_n b_n, ϵ_n and G_n was omitted due to the same configuration of each plate.

In this study, the water depth h is fixed at 10 m and the water density ρ is set to 1000 kg m^{-3}. For a representative porosity $\epsilon = 0.1$ and plate thickness $b = 0.1$ m, a wave frequency range of $f \in [0.016, 0.40]$ Hz yields a complex porosity parameter $G = G_r + \mathrm{i}G_i$ with $G_r \in [0.168, 10.611]$ and $G_i \in [0.018, 1.528]$. As indicated in Eq. (6), G is a function of several physical variables, including ϵ, b, h, and the wavenumber k. To simplify the parametric analysis, this study focuses on the integrated influence of G rather than examining the effects of each physical parameter individually.

3.1. Model validation

As indicated in Eq. (15), the mathematical expressions of the velocity potential are represented as infinite series. Therefore, it is necessary to verify their convergence to ensure both accuracy and computational efficiency.

The effect of the truncation parameter J in the vertical eigenfunction $Z_j(z)$ and Q in the auxiliary function $u_{n,q}(z)$ is examined, with the horizontal wave force $F_{e,n}$ selected as the target quantity for validation. For simplicity, its nondimensional form $F_{e,n}^* = |F_{e,n}|/(\rho g A)$ is used. Figs. 2(a)(b) and (c) present the frequency-domain results of $F_{e,n}^*$ for different truncation parameter J. It is observed from Fig. 2(a) that the present solution converges rapidly with increasing J. From the inset in Fig. 2(a), it can be seen that the value of $F_{e,1}^*$ remains almost unchanged when $J > 50$. A consistent trend for $F_{e,2}^*$ and $F_{e,3}^*$ can also be found in Figs. 2(b) and (c). For the truncation parameter Q, the results in Figs. 2(d)(e) and (f) also indicate that the value of $F_{e,n}^*$ converges quickly with the increasing of Q. These results demonstrate that the present solution achieves high computational efficiency. To ensure high accuracy in subsequent calculations, the $J = 70$ for $Z_j(z)$ and $Q = 6$ for $u_{n,q}(z)$ is adopted.

The dissipation coefficient D obtained by the direct method (i.e., Eq. (41)) and the indirect method (i.e., Eq. (44)) are compared to validate the correctness of the present analytical solution. The dissipation coefficients for different plate numbers with $L/h = 2$, $l/h = 0.5$, and $G = 0.5$ are calculated, as shown in Fig. 3. It can be seen that the values of D computed by the two methods under various conditions are in perfect agreement, verifying the accuracy of the present analytical model.

In addition, the present results are validated against those of Lee and Chwang (2000) to justify the present method. Lee and Chwang (2000) employed the least-squares method to obtain an accurate analytical solution for wave scattering by a single vertical thin porous barrier. The reflection and transmission coefficients calculated by the present method and the least-squares solution of Lee and Chwang (2000) for a bottom-standing porous barrier with $l/h = 0.75$ and different porosity parameters are compared in Fig. 4. It can be seen that the present results are in good agreement with those of Lee and Chwang (2000), confirming the consistency and stability of the present model.

3.2. Bragg scattering characteristics

The scattering characteristics of water waves by periodic porous plates are discussed in this subsection.

The reflection and transmission coefficients for solid and porous plate arrays with different numbers of plates are shown in Fig. 5. It can be observed that peaks in the reflection curves occur at nondimensional wavenumbers $kh = 1.45$, 3.11, and 4.59, and the peak heights increase with the number of plates. In fact, the appearance of these peaks results from the Bragg resonance effect. According to Bragg's law, maximum reflection occurs when the lattice constant is an integer multiple of half the wavelength (Bragg, 1912), i.e., $2L/\lambda = m$, where m is an integer and λ is the wavelength. If the horizontal axis kh is replaced by $2L/\lambda$, it can be found that the values corresponding to $kh = 1.45$, 3.11, and 4.59 are approximately $2L/\lambda = 1$, 2, and 3, respectively. The insets in Figs. 5(a), (b), and (c) confirm the presence of Bragg resonance. In addition, it can be seen that the porous plates exhibit weaker wave reflection compared to the solid plates.

Moreover, there are $N-2$ sub-harmonic peaks between two adjacent main resonance peaks. The appearance of these sub-harmonics results from Bragg resonance between any two plates within the array. Physically, these sub-harmonic peaks correspond to the multiple scattering

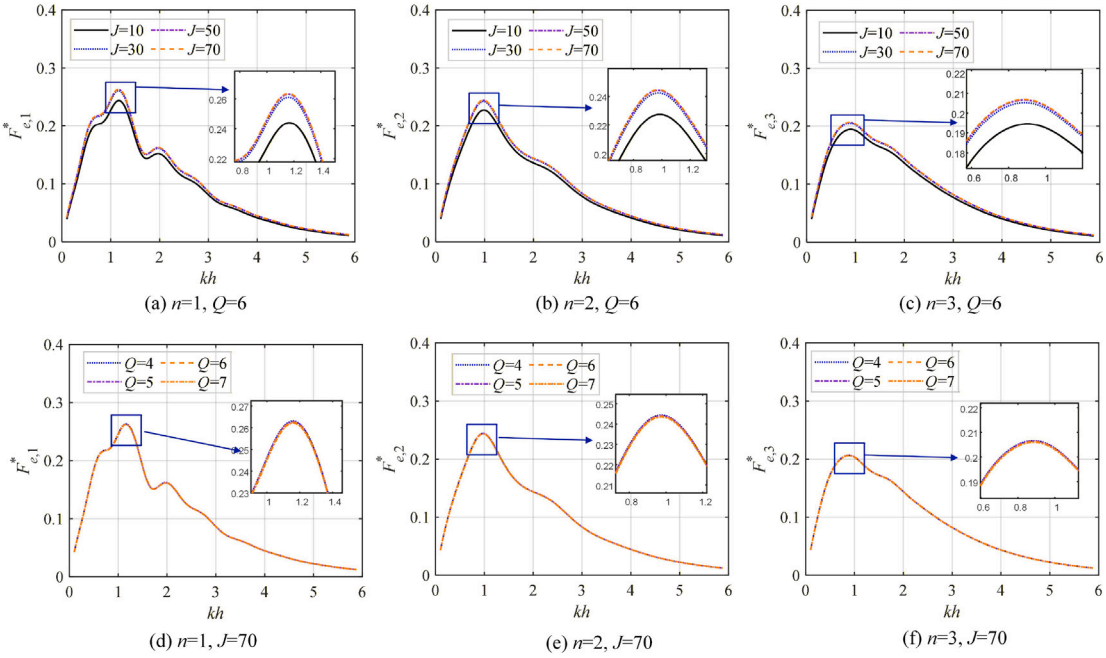

Fig. 2. Convergence analysis of truncation parameters J and Q for wave force $F^*_{e,n}$ with $L/h = 2$, $l/h = 0.5$, $G = 0.5$, and $N = 3$.

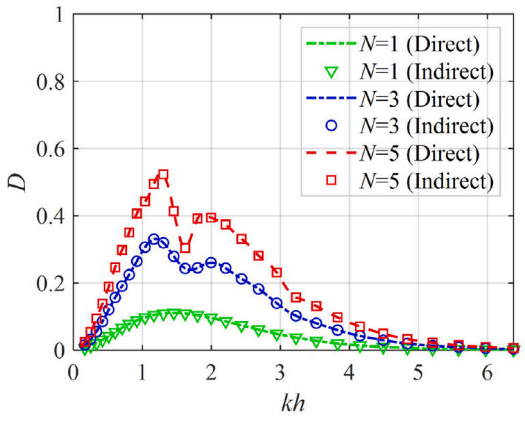

Fig. 3. Comparison of dissipation coefficient D computed by the direct method (from Eq. (41)) and indirect method (from Eq. (44)) at $L/h = 2, l/h = 0.5$, and $G = 0.5$ with different plate number N.

paths of the waves among the non-adjacent plates. For example, the distance between the first and third plates is $2L$, and that between the first and fourth plates is $3L$; these distances also satisfy the Bragg condition and lead to smaller resonance reflections (Kar et al., 2020; Jin et al., 2024b). However, it should be noted that these sub-harmonics are not expected to persist if disorder is introduced into the plate spacing, as random phase differences between the scattered waves would disrupt the constructive interference required for Bragg resonance.

For wave transmission, the transmission coefficient T decreases as the number of plates N increases, as shown in Figs. 5(d), (e), and (f). The minima of the transmission coefficients correspond to the Bragg resonance peaks observed in the reflection coefficients. Notably, the porous plates consistently exhibit lower transmission coefficients than the solid plates across the entire frequency range. This enhancement in wave attenuation is quantitatively illustrated by the insets in Figs. 5(d)–(f), which display the relative difference $\Delta T = (T_{porous} - T_{solid})/T_{solid}$. In the non-Bragg resonance regions, while the transmission coefficient of the solid plates approaches unity, ΔT remains significantly negative, indicating that the porous plates maintain substantial energy dissipation where solid plates fail to do so. Specifically, the maximum reduction in T reaches approximately 58% when $N = 10$. These results further confirm that the periodic porous plates possess a superior capability to dissipate wave energy through the combined effects of Bragg reflection and viscous damping.

Fig. 6 illustrates the spatial distributions of the normalized velocity potential amplitude, $|\phi(x,z)/\phi^I(0,0)|$, under the first-order Bragg resonance condition ($kh = 1.45$). The incident wave propagates from the left boundary. Figs. 6(a), (c), and (e) depict the results for solid plates, while Figs. 6(b), (d), and (f) correspond to the porous plate cases. As N increases, the reflection from the array becomes more pronounced, leading to a significant increase in the upstream potential amplitude. For the $N = 10$ solid plate case (Fig. 6e), a distinct standing wave pattern is observed in the upstream region ($x/h < -9$, prior to the first plate). The spacing between the intensified potential peaks (antinodes) matches the theoretical half-wavelength $\lambda/(2h) \approx 2.15$. This high-intensity pattern suggests that the incident wave is almost entirely reflected by the solid array. In contrast, comparing the left and right columns reveals that the porous plates yield lower upstream amplitudes due to partial wave transmission and energy dissipation. Consequently, the downstream wave amplitude is significantly attenuated. As shown in Fig. 6(f), the velocity potential on the lee side ($x/h > 9$) approaches zero, demonstrating that the periodic porous plate array provides a superior shielding effect for protecting downstream maritime structures.

Fig. 7 presents the horizontal wave force acting on the solid and porous plate arrays with six cells. It can be observed that the wave force is large at low frequencies (around $kh = 1.28$), whereas it becomes relatively small at higher frequencies. In addition, by replacing the abscissa kh with $2L/\lambda$, it can be seen that the wave force drops sharply when Bragg resonance occurs, as shown in the inset of Fig. 7(a). Furthermore, the wave force acting on the plates gradually decreases as the number of plates increases. This can be understood from the physical perspective that the wave amplitude is progressively reduced

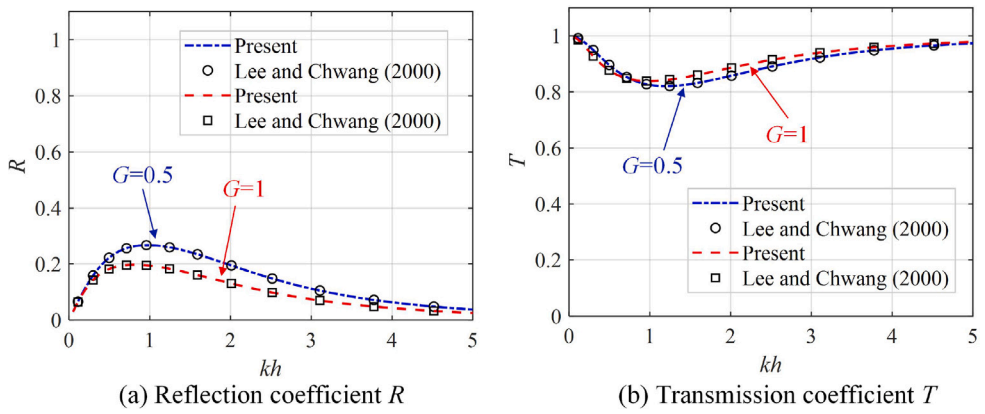

Fig. 4. Comparison of R, T between the present solution (lines) and that of Lee and Chwang (2000) (dots) at different porous parameters with $l/h = 0.75$ and $N = 1$.

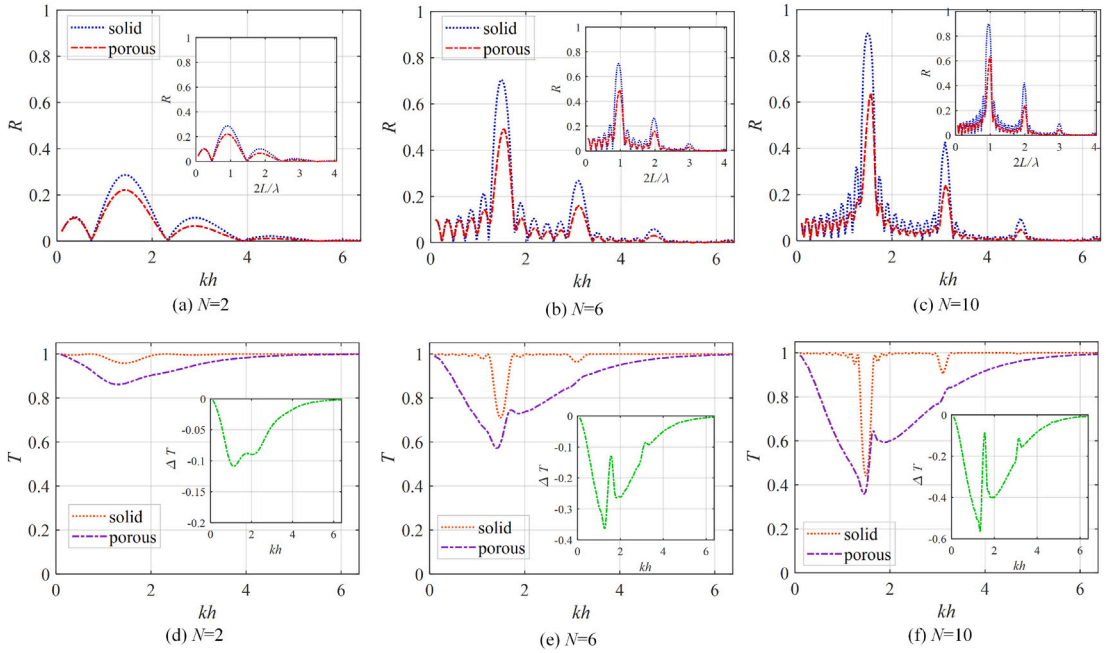

Fig. 5. Wave reflection and wave transmission by solid plates and porous plates with different numbers. The other parameters used for calculation are $l/h = 0.5$, $L/h = 2$, and $G = 0.5$ (0) for porous (solid) plates.

as the waves propagate through the plate array. More importantly, it is found that the porous plates experience smaller wave forces compared with the solid plates, indicating that the porous plates possess a stronger survivability under harsh marine conditions.

3.3. Effects of complex porosity parameter

The effects of the complex porosity parameter of the plates on wave energy reflection, transmission, and dissipation are discussed in this subsection.

First, the influence of the resistance induced by porosity in the absence of inertance, i.e., $\Im(G) = 0$, is investigated. Figs. 8(a), (b), and (c) respectively present the reflection coefficient R, transmission coefficient T, and dissipation coefficient D with increasing $\Re(G)$. In Fig. 8(a), the peak heights caused by Bragg resonance decrease as $\Re(G)$ increases, and the corresponding peak frequencies shift slightly toward higher values. For the transmission coefficient, its value does not continuously decrease with increasing G. The minimum transmission coefficient within the entire frequency range occurs at $G = 1$. Correspondingly, the envelope area of the dissipation coefficient curve is the largest when $G = 1$. This suggests that there exists an optimal G value that leads to the most effective attenuation of wave energy by the porous plate array. Additionally, it can be observed that as G increases, the dissipation coefficient curve shifts toward the low-frequency region, which indicates that larger G values are more effective for attenuating long waves.

Fig. 9 shows the effects of inertance in the absence of resistance, i.e., when G is a purely imaginary number. From Figs. 9(a) and (b), it can be observed that as $\Im(G)$ increases, the reflection coefficient decreases, while the transmission coefficient increases. This result can be explained intuitively from a physical perspective: as $\Im(G)$ increases, the plate becomes more permeable, allowing more fluid and energy

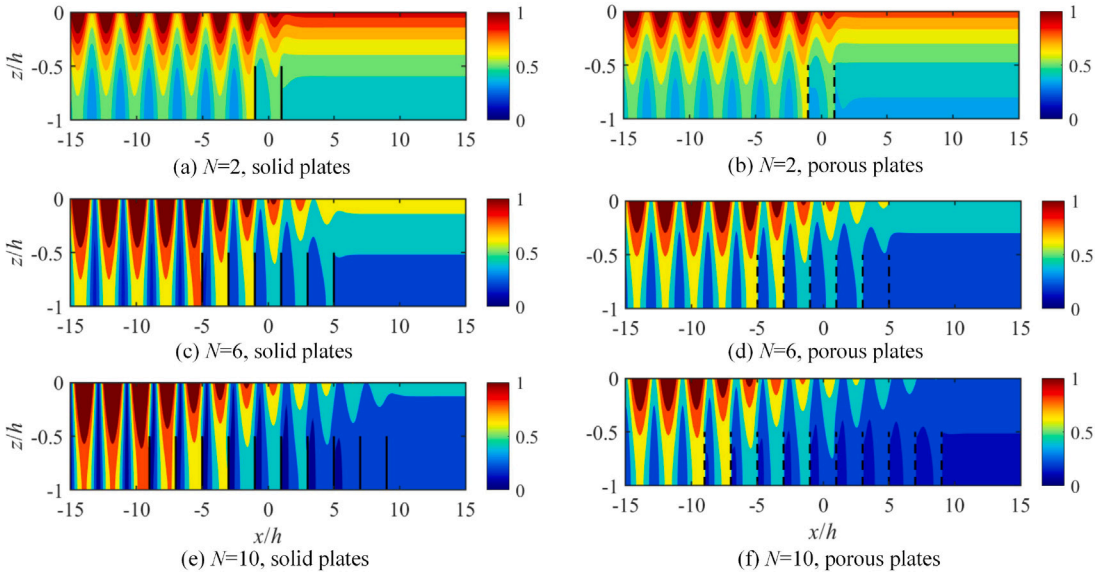

Fig. 6. Distribution of wave velocity field of incident wave interacting with solid plates (left column) and porous plates (right column) at $kh = 1.45$ (i.e., $2L/\lambda = 1$). The other parameter values are $l/h = 0.5$, $L/h = 2$, and $G = 0.5$ (0) for porous (solid) plates.

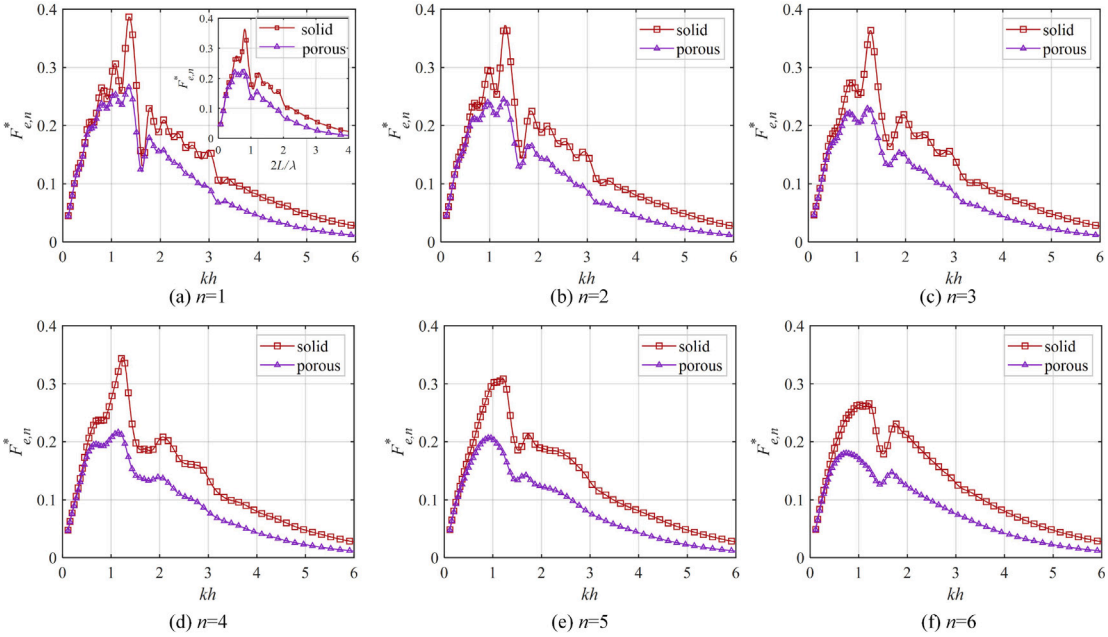

Fig. 7. Comparison of wave horizontal force acting on the solid plates and porous plates, with $l/h = 0.5$, $L/h = 2$, $N = 6$, and $G = 0.5$ (0) for porous (solid) plates.

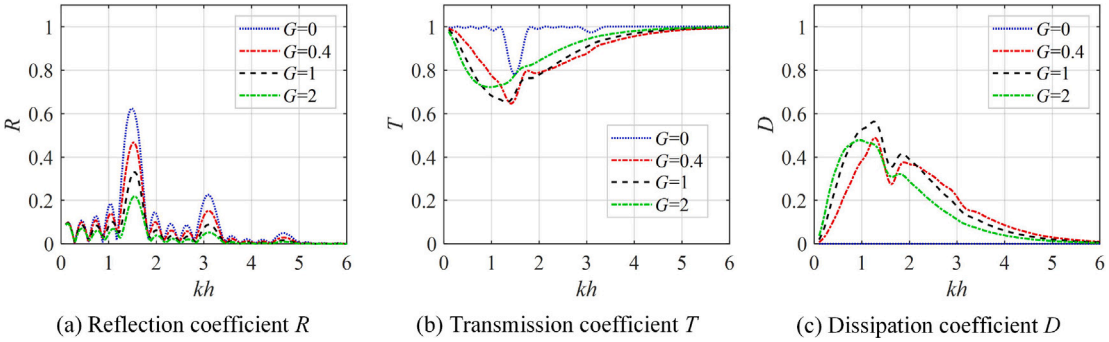

Fig. 8. Effects of resistance exerted by the porosity in the absence of the inertance, with $l/h = 0.5$, $L/h = 2$, and $N = 5$.

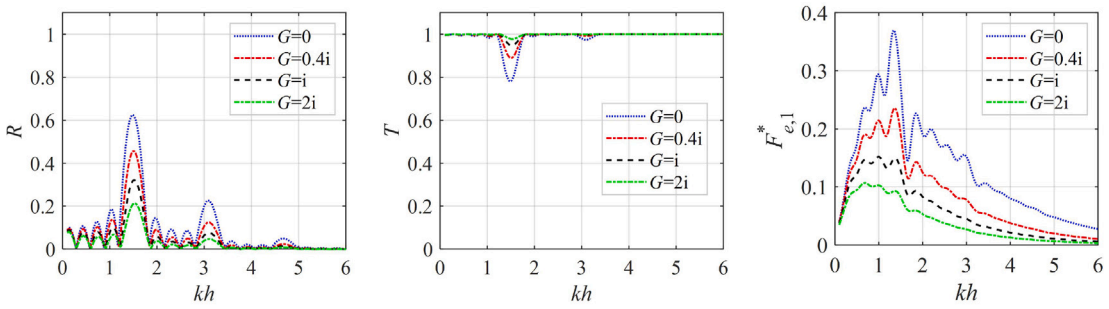

(a) Reflection coefficient R (b) Transmission coefficient T (c) Wave force $F^*_{e,1}$

Fig. 9. Effects of inertance exerted by the porosity in the absence of the resistance, with $l/h = 0.5$, $L/h = 2$, and $N = 5$.

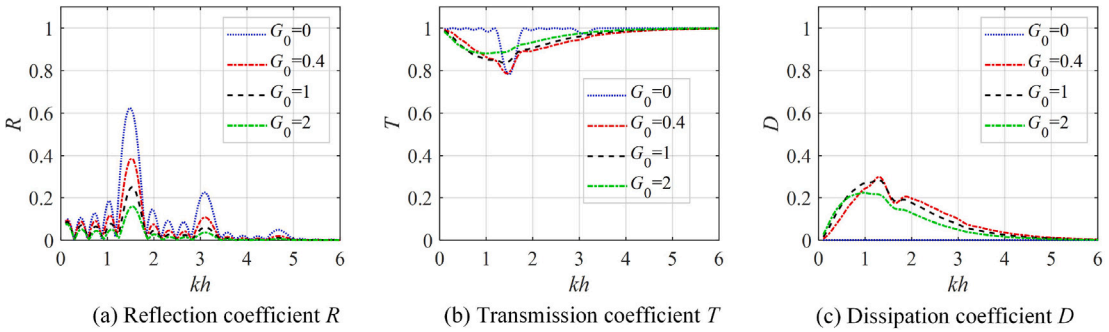

(a) Reflection coefficient R (b) Transmission coefficient T (c) Dissipation coefficient D

Fig. 10. Combined effects of resistance and inertia exerted by the porosity, with $l/h = 0.5$, $L/h = 2$, and $N = 5$.

to pass through; consequently, reflection weakens and transmission strengthens. When $\Im(G)$ approaches infinity, the plate becomes effectively non-existent, at which point the reflection coefficient approaches zero and the transmission coefficient approaches unity. As shown in Fig. 9(c), the wave force also decreases continuously with increasing $\Im(G)$.

Fig. 10 illustrates the combined effects of resistance and inertia induced by porosity. In this case, the resistance and inertial parameters are assumed to have equal magnitudes, and the porosity parameter is expressed as $G = G_0(1 + \mathrm{i})$, where $G_0 \in \mathbb{R}^+$. From Fig. 10(a), it can be observed that the reflection coefficient decreases monotonically as G_0 increases, exhibiting similar characteristics to those shown in Figs. 8 and 9(a). For the transmission coefficient, as shown in Fig. 10(b), it first decreases with increasing G_0 and then increases as G_0 continues to grow. The transmission coefficient reaches its minimum value at $G_0 = 0.4$. Correspondingly, the energy dissipation shows a consistent trend with varying G_0. The dissipation coefficient attains its maximum value at $G_0 = 0.4$, as shown in Fig. 10(c). Compared with the results in Fig. 8(c), it can be seen that the inclusion of inertial effects leads to a significant reduction in energy dissipation, which is not conducive to wave attenuation.

3.4. Effects of barrier length and lattice constant

In this subsection, we focus on the effect of the lattice scale (corresponding to the plate length and spacing) on wave propagation.

Fig. 11 shows the surface plots of the reflection, transmission, and dissipation coefficients as functions of the plate length and wavenumber. As seen in Fig. 11(a), an increase in plate length leads to stronger wave reflection. The height of the reflection peak caused by Bragg resonance increases and becomes broader with increasing plate length, and the minimum value of the sub-harmonic peak is no longer zero, as shown in the inset of Fig. 11(a). In Fig. 11(b), it can be observed that the transmission coefficient decreases with increasing plate length, and this trend is more pronounced in the long-wave region (i.e., at small kh). Regarding the dissipation coefficient, Fig. 11(c) illustrates that increasing the plate length significantly enhances wave energy attenuation. For $l/h = 0.8$ and $kh = 1$, the peak dissipation coefficient reaches approximately 90%. This trend suggests that while further increasing the plate length can lead to even higher energy dissipation, the system demonstrates a high-efficiency regime where the majority of incident energy is effectively dissipated by the porous structures. In addition, the dissipation coefficient decreases when Bragg resonance occurs, because most of the waves are reflected back and only a small portion propagates forward.

Fig. 12 shows the variations of the reflection, transmission, and dissipation coefficients with the lattice constant L, while the wavelength λ remains constant. Curves for different plate lengths are also presented. As seen in Fig. 12(a), the reflection coefficient exhibits an almost periodic variation as L changes. This behavior is governed by the mth order Bragg resonance condition, expressed as $2L/\lambda = m$ ($m = 1, 2, 3, \ldots$). As the lattice constant L increases, the phase difference between the waves reflected from successive plates changes periodically. When L satisfies the resonance condition, the reflected waves from all plates are in phase and superimpose constructively, resulting in a primary reflection peak. However, when the wavelength λ changes, the first-order Bragg resonance produces the strongest reflection, and the reflection decreases as the order m increases, as shown in Fig. 11(a). For the transmission and dissipation coefficients, they also exhibit nearly periodic variations with changing L, as shown in Figs. 12(b) and (c). Upon closer inspection, it can be observed that the dissipation coefficient decreases slightly with increasing L. Therefore, for wave attenuation in the ocean, it is most advantageous to exploit the first-order Bragg resonance to achieve strong wave reflection.

3.5. Hydrodynamic performance in irregular waves

To evaluate the engineering applicability of the proposed periodic porous structure in realistic marine environments, the monochromatic wave model presented in Section 2 is extended to irregular sea states.

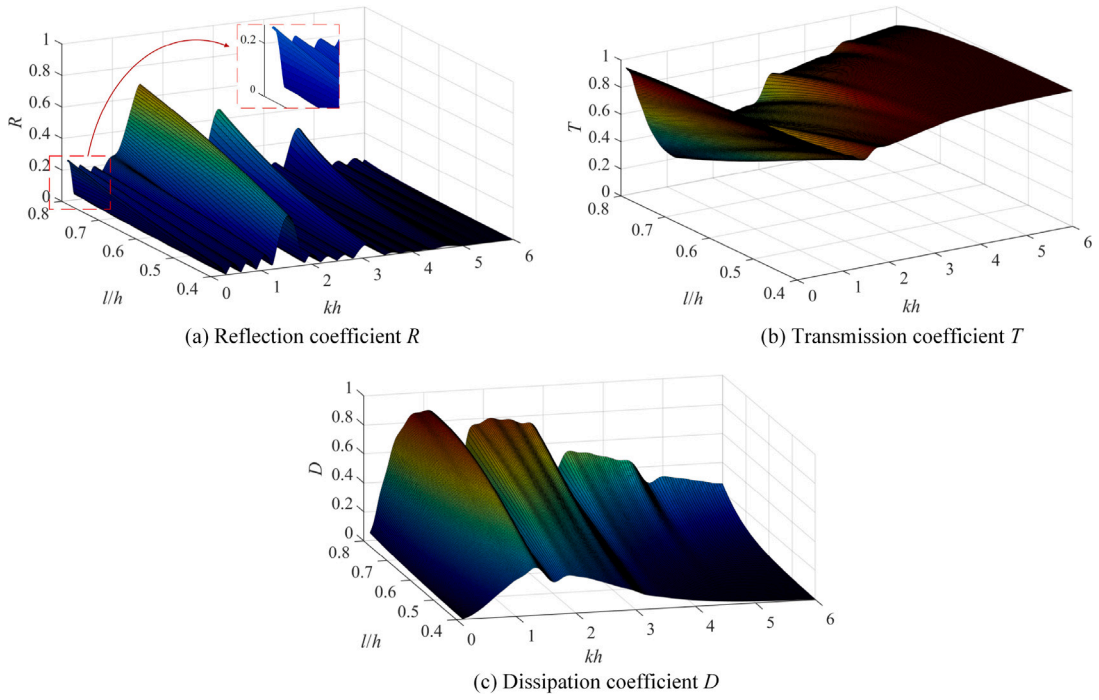

(a) Reflection coefficient R (b) Transmission coefficient T

(c) Dissipation coefficient D

Fig. 11. Variations of wave reflection, transmission, and energy dissipation with wavenumber kh at $L/h = 2$, $G = 0.5$, $N = 5$ for different plate lengths.

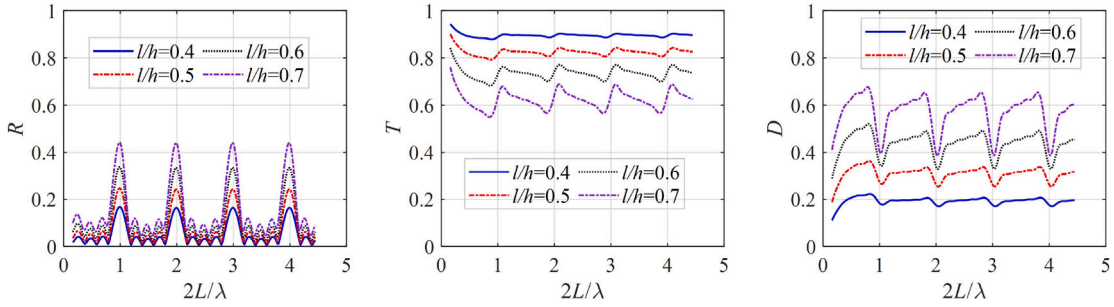

(a) Reflection coefficient R (b) Transmission coefficient T (c) Dissipation coefficient D

Fig. 12. Variations of wave reflection, transmission, and energy dissipation with the lattice constant L for different l when $kh = 2.5$, $G = 0.5$ and $N = 5$.

By applying the linear superposition principle, the reflection, transmission, and dissipation characteristics for each frequency component f are characterized by the coefficients $R(f)$, $T(f)$, and $D(f)$, respectively. Accordingly, the power spectral densities of the reflected, transmitted, and dissipated waves are defined as:

$$S_r(f) = R(f)^2 S_i(f), \quad S_t(f) = T(f)^2 S_i(f), \quad S_d(f) = D(f) S_i(f) , \tag{45}$$

where $S_i(f)$ denotes the incident wave energy density.

The JONSWAP spectrum, widely adopted for North Sea conditions, is employed to represent the incident random waves:

$$S_i(f) = \frac{\alpha g^2}{(2\pi)^4 f^5} \exp\left[-\frac{5}{4}\left(\frac{f_p}{f}\right)^4\right] \gamma^{\exp\left[-\frac{(f-f_p)^2}{2\sigma^2 f_p^2}\right]} , \tag{46}$$

where f_p is the peak frequency, H_s is the significant wave height, γ is the peak enhancement factor, and σ is the peak shape coefficient ($\sigma = 0.07$ for $f \le f_p$ and $\sigma = 0.09$ for $f > f_p$). The Phillips constant α is given by:

$$\alpha = \frac{5}{16} \frac{(2\pi)^4 H_s^2 f_p^4}{g^2} \frac{1}{1 - 0.287 \ln \gamma} . \tag{47}$$

To quantify the overall hydrodynamic performance across the entire frequency range, the frequency-averaged reflection, transmission, and dissipation coefficients ($\overline{C_r}$, $\overline{C_t}$, and $\overline{C_d}$) are defined based on the zero-th moments of the respective spectra:

$$\overline{C_r} = \sqrt{\frac{m_{0,r}}{m_{0,i}}}, \quad \overline{C_t} = \sqrt{\frac{m_{0,t}}{m_{0,i}}}, \quad \overline{C_d} = \frac{m_{0,d}}{m_{0,i}} , \tag{48}$$

where $m_{0,j} = \int_0^\infty S_j(f)\mathrm{d}f$ (with $j \in \{i, r, t, d\}$) represents the zero-th moment of the incident, reflected, transmitted, and dissipated wave spectra, respectively.

Fig. 13 illustrates the hydrodynamic performance of the porous-plate array across different spectral bandwidths. The top row depicts the incident wave spectra for peak enhancement factors of $\gamma = 1$, 3.3, and 10. The bottom row displays the corresponding reflected, transmitted, and dissipated energy spectra. All spectra are normalized by f/f_p, where $f_p = 0.14$ Hz, which corresponds to the first-order Bragg resonance frequency. In the figures, also shown the incident significant wave height, H_s, peak frequency f_p, and the values of frequency-averaged reflection coefficient $\overline{C_r}$, transmission coefficient $\overline{C_t}$ and dissipation coefficient $\overline{C_d}$.

As shown in Fig. 13, the dissipation spectral density S_d follows a similar distribution to the incident spectrum, peaking at $f/f_p = 1$.

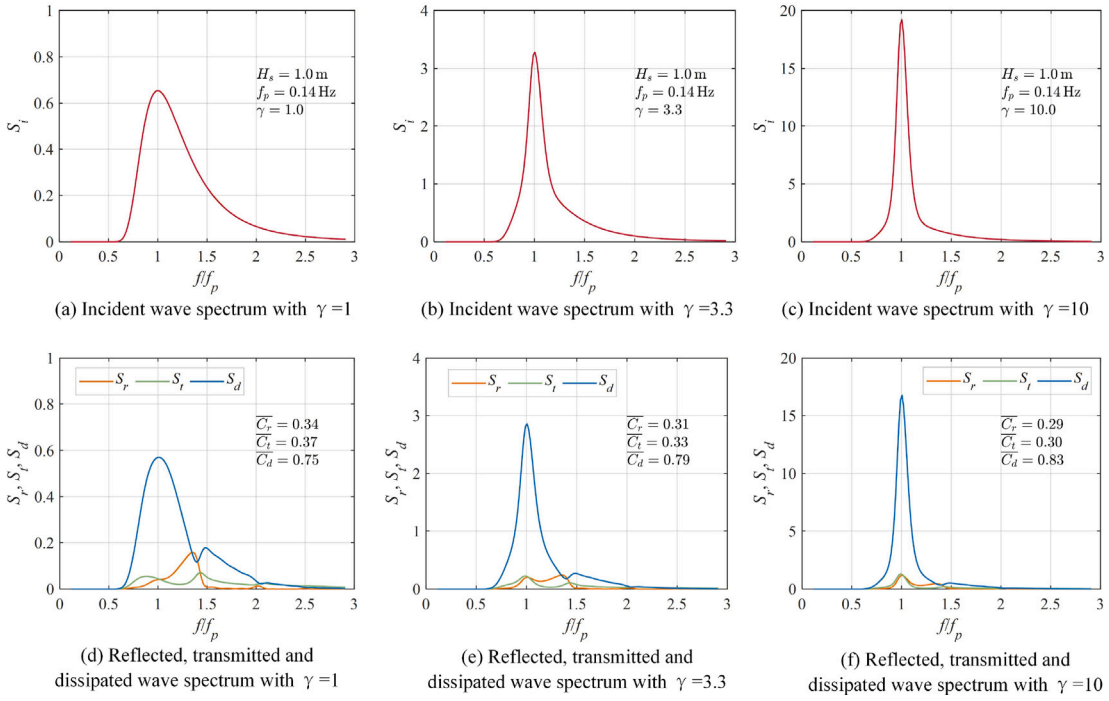

(a) Incident wave spectrum with γ =1 (b) Incident wave spectrum with γ =3.3 (c) Incident wave spectrum with γ =10

(d) Reflected, transmitted and dissipated wave spectrum with γ =1 (e) Reflected, transmitted and dissipated wave spectrum with γ =3.3 (f) Reflected, transmitted and dissipated wave spectrum with γ =10

Fig. 13. Spectra for (a) broad, (b) ordinary, and (c) narrow incident wave conditions. Corresponding reflected, transmitted, and dissipated wave spectra for (d) broad, (e) ordinary, and (f) narrow incident waves. Parameters: $l/h = 0.8$, $G = 0.5$, $L/h = 2$, and $N = 5$.

As γ increases (indicating a narrower bandwidth), the spectral peaks become more pronounced, and the frequency-averaged dissipation coefficient $\overline{C_d}$ increases accordingly. For a Pierson–Moskowitz spectrum ($\gamma = 1$), the structure dissipates approximately 75% of the incident wave energy, rising to 83% for a narrow-banded spectrum ($\gamma = 10$). Notably, the frequency-averaged transmission coefficient $\overline{C_t}$ remains below 50% across all tested cases, satisfying the criteria for effective wave attenuation (Dai et al., 2018; Jin et al., 2022). These results confirm that periodic porous plates provide robust wave protection in realistic, stochastic marine environments.

4. Conclusion

In this study, a novel wave attenuation system composed of periodically arranged porous thin plates has been systematically investigated. Unlike existing models that focus solely on either impermeable structures or non-periodic dissipation, this work integrates Bragg scattering with porous-induced energy dissipation within a single, unified analytical framework. The boundary-value problem was rigorously formulated using linear potential flow theory and solved via the eigenfunction expansion method, supplemented by the polynomial Galerkin method to resolve velocity singularities at the thin-plate edges. The rigorous validation strategy, including convergence tests, energy conservation, and comparison with a known analytical solution, was implemented.

The parametric analysis was conducted to examine the characteristics of periodic porous plates, including free-surface wave amplitude, wave dissipation performance, and wave force. The main findings are summarized as follows:

(1) Bragg resonance can be triggered by periodic porous plates, and its peak reflection increases with the number of plates.

(2) Porous plates exhibit better wave-sheltering performance than solid plates, particularly in non-Bragg resonance frequency bands.

(3) The resistance effect induced by porosity can effectively dissipate wave energy, and near-complete dissipation is attainable under specific parameter configurations.

(4) The peak reflection of Bragg resonance depends on the wave conditions; it generally diminishes as the relative wavelength decreases, whereas the magnitude of the resonance peaks exhibits a low sensitivity as the lattice constant changes.

This study presents a promising approach for developing cost-effective and environmentally friendly devices for wave attenuation, which could significantly contribute to coastal erosion mitigation and infrastructure protection. However, several limitations of the current model should be acknowledged. First, the complex porosity parameter G is treated as a constant independent of wave amplitude; in practical engineering scenarios, laboratory experiments are essential to calibrate this coefficient, particularly to account for potential nonlinear effects under high-velocity flow. Furthermore, this study assumes the plates to be rigid and stationary. Future research incorporating structural hydroelasticity (flexible plates) or the dynamic response of floating/oscillating systems would provide a more comprehensive understanding of these periodic structures in real-world sea states.

CRediT authorship contribution statement

Huaqing Jin: Writing – original draft, Formal analysis, Conceptualization. **Siming Zheng:** Formal analysis, Supervision, Writing – review & editing. **Sichao Qu:** Data curation, Writing – review & editing. **Xinyi Xie:** Writing – review & editing, Funding acquisition. **Haicheng Zhang:** Funding acquisition, Supervision, Writing – original draft, Writing – review & editing. **Xiaofan Li:** Supervision, Methodology, Funding acquisition.

Declaration of competing interest

The authors declare the following financial interests/personal relationships which may be considered as potential competing interests: Xiaofan Li reports financial support was provided by The University of Hong Kong. Haicheng Zhang reports financial support was provided by Hunan University. If there are other authors, they declare that they

have no known competing financial interests or personal relationships that could have appeared to influence the work reported in this paper

Acknowledgments

The authors are grateful for the funding from The University of Hong Kong Seed Fund for Basic Research for New Staff, The science and technology innovation Program of Hunan Province (No. 2025RC3102), and XJTLU Research Development Funding (Grant No. RDF-24-02-085).

Data availability

The datasets generated and analyzed during the current study are available from the corresponding author on reasonable request.

References

Bragg, W.L., 1912. The specular reflection of X-rays. Nature 90 (2250), 410–410.
Bragg, W.H., Bragg, W.L., 1913. The reflection of X-rays by crystals. Proc. R. Soc. Lond. Ser. A Contain. Pap. A Math. Phys. Character 88 (605), 428–438.
Chanda, A., Pramanik, S., 2023. Effects of a thin vertical porous barrier on the water wave scattering by a porous breakwater. Phys. Fluids 35 (6).
Chang, H.-K., Liou, J.-C., 2007. Long wave reflection from submerged trapezoidal breakwaters. Ocean Eng. 34 (1), 185–191.
Cho, Y.-S., Lee, J.-I., Kim, Y.-T., 2004. Experimental study of strong reflection of regular water waves over submerged breakwaters in tandem. Ocean Eng. 31 (10), 1325–1335.
Cui, J., Cong, L., Teng, B., 2023. An eigenvalue method based on the integral equation with a Rankine source for the band structure of water surface waves over periodic scatterers. Ocean Eng. 283, 114911.
Dai, J., Wang, C.M., Utsunomiya, T., Duan, W., 2018. Review of recent research and developments on floating breakwaters. Ocean Eng. 158, 132–151.
Davies, A., 1982. The reflection of wave energy by undulations on the seabed. Dyn. Atmos. Oceans 6 (4), 207–232.
Falnes, J., Kurniawan, A., 2020. Ocean Waves and Oscillating Systems: Linear Interactions Including Wave-Energy Extraction, vol. 8, Cambridge University Press.
Halvorson, B., Huang, Z., 2024. Study of effects of perforation layouts on wave energy dissipation caused by a submerged perforated breakwater in front of a vertical seawall. Ocean Eng. 311, 119025.
Han, M., Wang, C., 2022. Potential flow theory-based analytical and numerical modelling of porous and perforated breakwaters: A review. Ocean Eng. 249, 110897.
Heathershaw, A., 1982. Seabed-wave resonance and sand bar growth. Nature 296 (5855), 343–345.
Hsu, T.-W., Chang, H.-K., Tsai, L.-H., Li, Y.-X., 2001. Experiments on the bragg reflection of waves by different types of artificial bars. In: ISOPE International Ocean and Polar Engineering Conference. ISOPE, pp. ISOPE–I.
Ji, C.-Y., Chen, X., Cui, J., Gaidai, O., Incecik, A., 2016. Experimental study on configuration optimization of floating breakwaters. Ocean Eng. 117, 302–310.
Jin, H., Zhang, H., Lu, Y., Xu, D., 2024a. Floating periodic pontoons for broad bandgaps of water waves. Appl. Math. Mech. 45 (11), 1913–1928.
Jin, H., Zhang, H., Xu, D., Liu, C., Xu, S., 2022. Analytical investigation on wave attenuation performance of a floating breakwater with nonlinear stiffness. Ocean Eng. 243, 110160.
Jin, H., Zhang, H., Zheng, S., Xu, D., 2024b. Characteristics of a two-dimensional periodic wave energy converter array. Renew. Energy 222, 119834.
Kar, P., Sahoo, T., Meylan, M., 2020. Bragg scattering of long waves by an array of floating flexible plates in the presence of multiple submerged trenches. Phys. Fluids 32 (9).
Kumaran, V., Venkateswarlu, V., Manu, 2025. Hydrodynamic performances of vertical wall type breakwater with slotted barriers: a physical and numerical approach. Sci. Rep. 15 (1), 25224.
Kushwaha, M.S., Halevi, P., Dobrzynski, L., Djafari-Rouhani, B., 1993. Acoustic band structure of periodic elastic composites. Phys. Rev. Lett. 71 (13), 2022.
Lee, M., Chwang, A., 2000. Scattering and radiation of water waves by permeable barriers. Phys. Fluids 12 (1), 54–65.
Li, Y., Liu, Y., Teng, B., 2006. Porous effect parameter of thin permeable plates. Coast. Eng. J. 48 (4), 309–336.
Liang, H., Zheng, S., Shao, Y., Cong, P., Greaves, D., 2023. Wave interactions with a cylinder surrounded by an arc-shaped breakwater. J. Fluids Struct. 123, 104021.
Liu, Y., Li, H.-j., Zhu, L., 2016. Bragg reflection of water waves by multiple submerged semi-circular breakwaters. Appl. Ocean Res. 56, 67–78.
Liu, H.-W., Xie, W.-J., Xie, J.-J., Ning, D., 2025. Zero reflections of water surface gravity waves induced by a finite periodic array of artificial bars. Phys. Fluids 37 (3).
Ma, G., Sheng, P., 2016. Acoustic metamaterials: From local resonances to broad horizons. Sci. Adv. 2 (2), e1501595.
Mei, C.C., 1985. Resonant reflection of surface water waves by periodic sandbars. J. Fluid Mech. 152, 315–335.
Molin, B., 2011. Hydrodynamic modeling of perforated structures. Appl. Ocean Res. 33 (1), 1–11.
Neelamani, S., Al-Salem, K., Taqi, A., 2017. Experimental investigation on wave reflection characteristics of slotted vertical barriers with an impermeable back wall in random wave fields. J. Waterw. Port Coast. Ocean. Eng. 143 (4), 06017002.
Ning, D., Zhang, S., Chen, L., Liu, H.-W., Teng, B., 2022. Nonlinear Bragg scattering of surface waves over a two-dimensional periodic structure. J. Fluid Mech. 946, A25.
Porter, R., Evans, D., 1995. Complementary approximations to wave scattering by vertical barriers. J. Fluid Mech. 294, 155–180.
Porter, R., Porter, D., 2003. Scattered and free waves over periodic beds. J. Fluid Mech. 483, 129–163.
Praveen, K., Venkateswarlu, V., Karmakar, D., 2022. Hydroelastic response of floating elastic plate in the presence of vertical porous barriers. Ships Offshore Struct. 17 (2), 457–471.
Qiao, D., Feng, C., Yan, J., Liang, H., Ning, D., Li, B., 2020. Numerical simulation and experimental analysis of wave interaction with a porous plate. Ocean Eng. 218, 108106.
Qiao, W., Wang, K.-H., Sun, Y., 2018. Scattering of water waves by a floating body with two vertically attached porous walls. J. Eng. Mech. 144 (2), 04017162.
Reyes, C.C., Walker, M., Huang, Z., Cross, P., 2024. A dual-function design of an oscillating water column integrated with a slotted breakwater: A wave flume study. Energies 17 (15), 3848.
Sahoo, G., Venkateswarlu, V., Martha, S., 2025. Mitigation of structural response on a floating elastic plate in the presence of multiple porous structures. Appl. Ocean Res. 154, 104412.
Suh, K.-D., Kim, Y.W., Ji, C.-H., 2011. An empirical formula for friction coefficient of a perforated wall with vertical slits. Coast. Eng. 58 (1), 85–93.
Torres, M., Adrados, J., Montero de Espinosa, F., 1999. Visualization of Bloch waves and domain walls. Nature 398 (6723), 114–115.
Vijay, K., Venkateswarlu, V., Sahoo, T., 2021. Bragg scattering of surface gravity waves by an array of submerged breakwaters and a floating dock. Wave Motion 106, 102807.
Wu, Q., Feng, X., Dong, Y., 2024. Nonlinear Bragg resonance of focused wave groups by periodic seabed topography. Phys. Fluids 36 (12).
Wu, B., Jiang, W., Jiang, J., Zhao, Z., Tang, Y., Zhou, W., Chen, W., 2024. Wave manipulation in intelligent metamaterials: recent progress and prospects. Adv. Funct. Mater. 34 (29), 2316745.
Xu, W., Tao, A., Zeng, J., Fan, J., Liu, J., Hou, P., Zheng, J., 2025. Experimental investigation on wave attenuation of oyster castles in optimized layout based on Bragg resonance. Ocean Eng. 321, 120426.
Yablonovitch, E., Gmitter, T., 1989. Photonic band structure: The face-centered-cubic case. Phys. Rev. Lett. 63 (18), 1950.
Yu, X., 1995. Diffraction of water waves by porous breakwaters. J. Waterw. Port Coast. Ocean. Eng. 121 (6), 275–282.
Yu, X., Chwang, A.T., 1994. Wave motion through porous structures. J. Eng. Mech. 120 (5), 989–1008.
Zheng, S., Michele, S., Liang, H., Meylan, M.H., Greaves, D., 2022. Wave power extraction from a floating elastic disk-shaped wave energy converter. J. Fluid Mech. 948, A38.
Zhu, S., Chwang, A.T., 2001. Analytical study of porous wave absorber. J. Eng. Mech. 127 (4), 326–332.
Zhu, S., Zhao, X., Han, L., Zi, J., Hu, X., Chen, H., 2024. Controlling water waves with artificial structures. Nat. Rev. Phys. 6 (4), 231–245.